ADVANCED MATERIALS
www.advmat.de

An All-Organic Self-Powered Photodetector with Ultraflexible Dual-Polarity Output for Biosignal Detection

*Tingting Yan, Ziqing Li, Fa Cao, Jiaxin Chen, Limin Wu, and Xiaosheng Fang**

Endowing photodetectors with mechanically flexibility and actual functionality are current research issues in developing optoelectronic devices. However, rigid metal-based or metal-oxide-based electrodes remain a block to the realization of ultraflexible electronics. Thus, an ultraflexible all-organic photodetector (all-OPD) is designed by innovatively introducing symmetrical organic electrodes PH1000/PH1000 to substitute the widely applied indium-doped tin oxide (ITO)/Ag electrodes. Specifically, this all-OPD exhibits a high self-powered responsivity (*R*) of over 100 mA W^{-1} among 500–600 nm and the photocurrent remains about 80% of the original performance after being bent 20 000 circles, and can output steady biosignals for photo-plethysmography (PPG) application. More importantly, this all-OPD outputs dual-polarity photocurrent as it is flipped or folded. Benefitting from the ordered phase distribution and designed Schottky barrier heights, the photogenerated holes will be transferred and collected by nearer electrode, while electrons will be trapped in the thick bulk heterojunction (BHJ) as a result of the long channel. This work offers a new avenue toward developing a multifunctional and ultraflexible all-OPD with a straightforward all-solution method, and it is expected to be more compatible in complex application scenarios.

1. Introduction

Abundant organic semiconductors have been developed recently, thus, offer us more options in designing organic electronic devices.[1–4] The energy levels and spectral absorption range of organic semiconductors can be easily regulated by molecular design.[5–7] In addition, organic semiconductors have unique advantages due to their mechanical flexibility, low cost, and ease of processing, which have great potential in portable wearable electronics.[8,9]

T. Yan, F. Cao, J. Chen, L. Wu, X. Fang
Department of Materials Science
Fudan University
Shanghai 200433, P. R. China
E-mail: xshfang@fudan.edu.cn
Z. Li, X. Fang
Institute of Optoelectronics
Fudan University
Shanghai 200433, P. R. China
L. Wu
College of Chemistry and Chemical Engineering
Inner Mongolia University
Hohhot 010021, P. R. China
The ORCID identification number(s) for the author(s) of this article can be found under https://doi.org/10.1002/adma.202201303.

DOI: 10.1002/adma.202201303

An organic photodetector (OPD), with organic semiconductors as photosensitive layer, has proved to rival that of a low-noise silicon photodetector, almost in all metrics[10] and has promising applications in health monitoring and image sensing.[11–13] In the meantime, flexible organic semiconductors are advantageous substitutes for inorganic semiconductors in wearable electronics because conformal thin-film devices can be manufactured with them, therefore, can better adhere and fit human skin.[14,15] Although organic semiconductors can make up for the poor flexibility of inorganic semiconductors to some extent, the metal-based or metal oxide electrodes in OPD remain a block to the realization of ultraflexible devices.[13] Simultaneously, metal-based or metal-oxide-based electrodes require vacuum thermal evaporation or electron beam deposition techniques that will complex the preparation process and increase production costs.[15] Introducing intrinsic flexible organic electrodes may help solve the above mentioned problems. The polymer conductor poly(3,4-ethylenedioxythiophene):poly(styrenesulfonate), PH1000 (PH1000) with superb transmittance and conductivity, which can be fabricated by a simple solution method, has proved to be the most promising electrode in skin-like wearable electronics.[1]

Dual-polarity photocurrent response endows optoelectronic devices with multifunctional characteristics that have proved to be applied in switchable light imaging, optical communication, and spectral bands' distinction.[16–19] While traditional p–n junction photodiodes should obey the physical principles of the unidirectional current migration, hence dual-polarity photocurrent response in the previous researches was realized by taking advantage of the concomitance among photovoltaic, photo-electrochemical, and photo-thermoelectric effects,[16,17,20,21] which has a high demand in selecting materials and fabricating devices. While in organic semiconductor systems, donors and acceptors blended to form interpenetrating bulk-heterojunction (BHJ) networks,[22] by reasonably designing the work functions of electrodes, migrations of electrons/holes can be effectively regulated thus can easily switch the polarity of electronic signals.[23,24] Distinctive characteristics of BHJ in OPD inspired us a straightforward and low-cost way in developing dual-polarity photocurrent response optoelectronic devices.

In this work, we introduced transparent organic electrodes PH1000/PH1000 to fabricate an all-organic photodetector (all-OPD) with a vertically aligned structure PH1000/poly(3,4-ethylenedioxythiophene):poly(styrenesulfonate), Al 4083

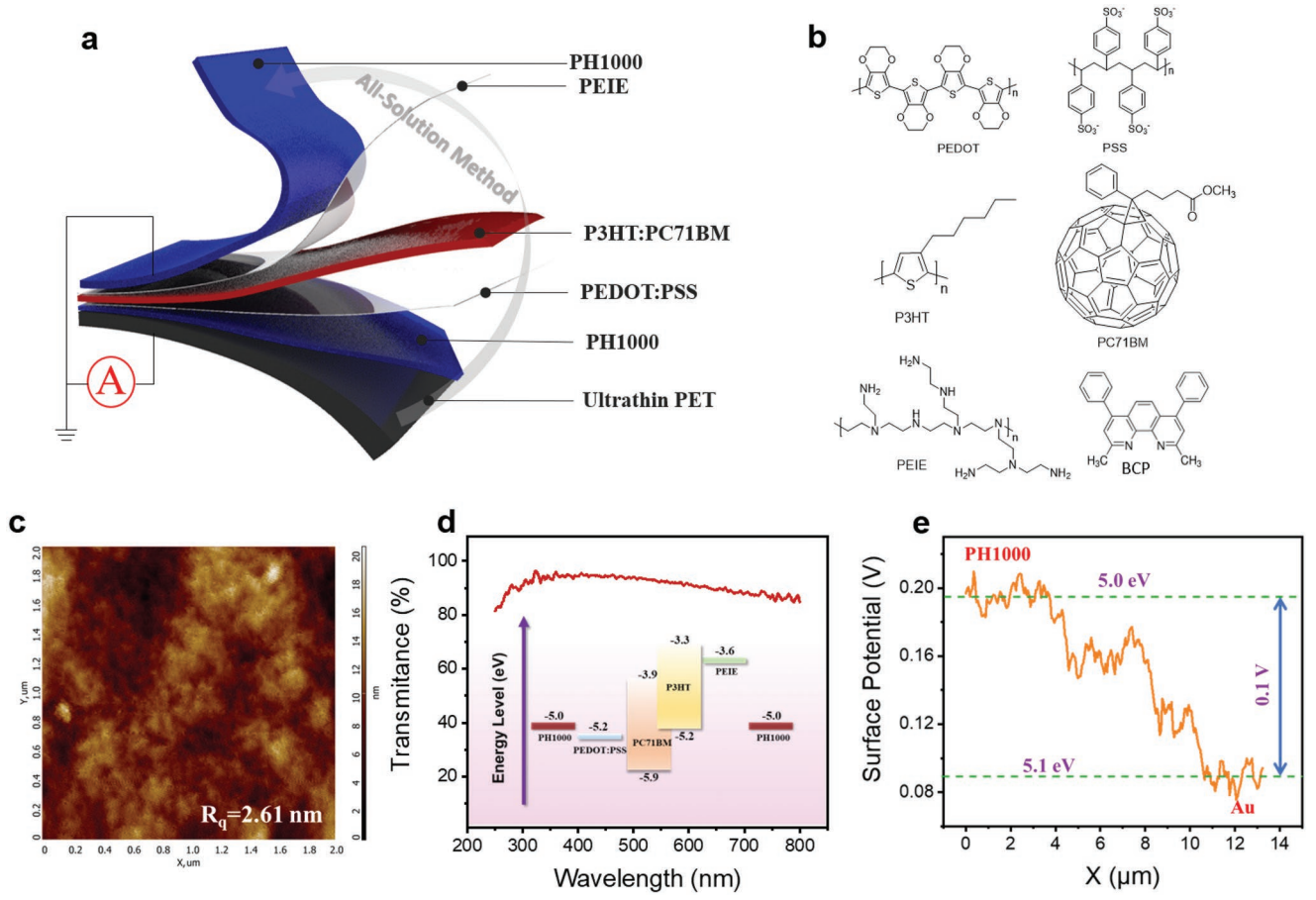

Figure 1. Device structure of the all-OPD and properties of PH1000. a) Device structure of the all-OPD, top PH1000 was connected to ground. b) Chemical structures of each layer. c) Surface morphology of PH1000 film. d) Transmittance of PH1000 and energy levels of each layer. e) Surface potential of PH1000 by utilizing Au as a reference.

(PEDOT:PSS)/poly(3-hexylthiphene) (P3HT):phenyl-C71-butyric-acid-methyl ester (PC71BM)/polyethylenimine ethoxylated (PEIE)/PH1000 that obtained a high self-powered responsivity (R) of more than 100 mA W^{-1} among 500–600 nm. Interestingly, by virtue of this device configuration, the polarity of the outputting photocurrent was changed as we flipped over or folded our all-OPD. The polarity of net current depended on the illumination position, where more photogenerated charge carriers would flow to and be collected by the nearer electrode. Two possible applications that may result from this effect were position monitoring and motion detections, which can be realized by detecting the electric signals as rotating or folding the all-OPD. Meanwhile, excellent flexibility of this device offers more application possibilities; biosignals were detected by sticking this soft all-OPD on finger pulp combined with a red light-emitting diode (LED). Given the simplicity of the device structure and fabricating process, this all-OPD will have great application potential in realizing multifunctional, portable, and wearable electronic devices.

2. Results and Discussion

Here, 500 nm bulk heterojunction was formed with the blends of organic semiconductor donor P3HT and acceptor PC71BM (Figure S1, Supporting Information) which acted as the photosensitive layer.[5,25] As schematically shown in **Figure 1**a, vertical sandwich structure was adopted to build a photodetector, where a photosensitive layer sits between the top and bottom electrodes and the total thickness of the device was about 30 μm. Chemical structures of each layer are listed in Figure 1b. PEDOT:PSS and PEIE were inserted to optimize contact between photosensitive layer and electrodes.[26–28]

In order to obtain an all-OPD with intrinsic flexibility, organic electrodes PH1000/PH1000 were introduced to substitute conventional rigid indium-doped tin oxide (ITO)/Ag electrodes in P3HT:PC71BM-based system (see Experimental Section for details). Smooth PH1000 films with a roughness of 2.61 nm were formed by a solution method on an ultrathin poly(ethylene terephthalate) (PET) substrate as a bottom electrode and on PEIE layer as a top electrode (Figure 1c). Additionally, PH1000 film was transparent enough, where nearly over 90% incident light around 250–800 nm can be transmitted from either top PH1000 electrode or bottom PH1000 electrode to photosensitive layers (Figure 1d); thus, the light loss arose from the reflection of the electrode would be minimized. The work function of PH1000 was determined to be −5.0 eV by Kelvin probe in air (Figure 1e; Figure S2, Supporting Information). Energy band diagrams of different layers were listed

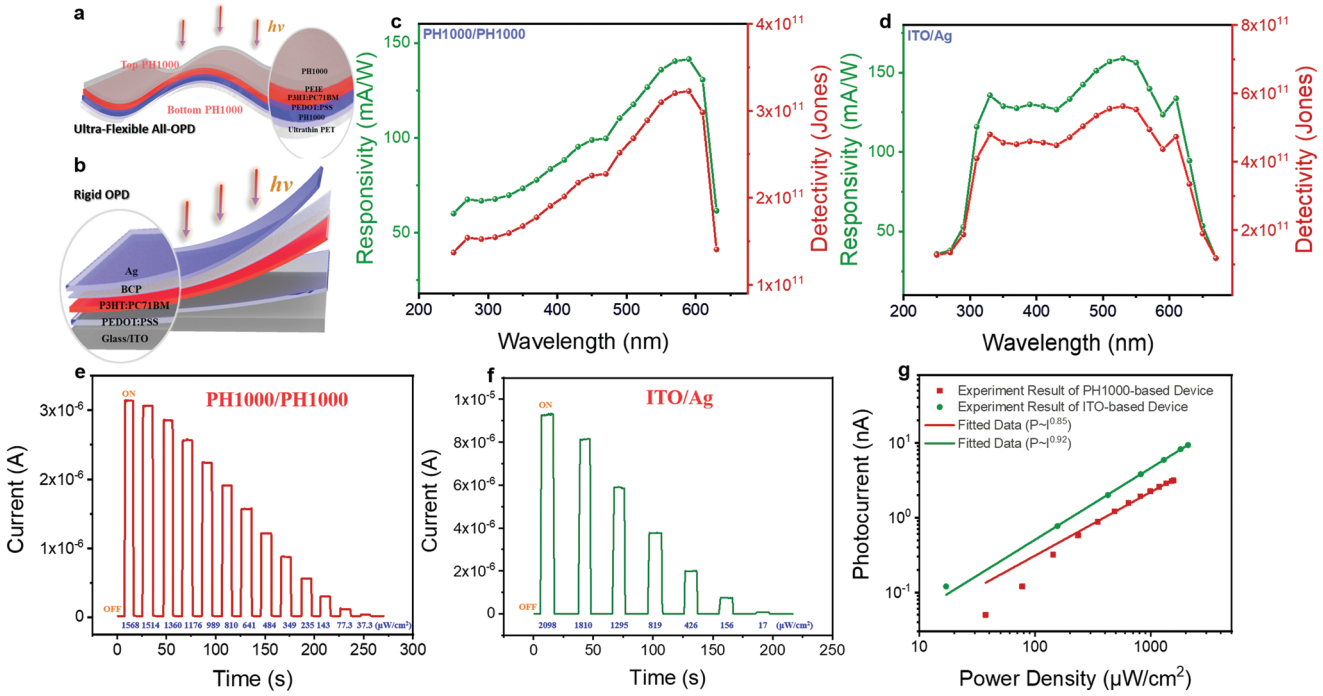

Figure 2. Optoelectronic properties of rigid OPD based on ITO/Ag electrodes and the flexible all-OPD based on PH1000/PH1000 electrodes. a,b) Device structure of ultraflexible OPD with PH1000/PH1000 as electrodes (a) and rigid OPD with ITO/Ag as electrodes (b). c,d) *R* and *D* of the ultraflexible all-OPD (c) and the rigid OPD (d). e,f) *I*–*t* curves under different illumination intensities of the ultraflexible all-OPD (e) and the rigid OPD (f). g) Photocurrent variation along with the power density.

to help us understand the migrations of the photogenerated carriers of the all-OPD (Figure 1d). A strong Schottky barrier may be created after semiconductor contacted electrodes due to the large energy level difference between PH1000 (−5.0 eV) and lowest unoccupied molecular orbital (LUMO) of PC71BM (−3.9 eV) where band bending effect would appear.

The all-OPD was successfully prepared with the device configuration PET/PH1000/PEDOT:PSS/P3HT:PC71BM/PEIE/PH1000 (**Figure 2**a). The evolution of sheet resistances of PET/PH1000 was tested as they were bending 0°, 90°, and 180°, as shown in Figure S3 (Supporting Information), and it was found that PET/PH1000 almost depicted the same resistance of its original value upon bending strain, which indicated that PET/PH1000 has superiority in prospect of practical application in flexible device. Optoelectronic properties of the ultraflexible all-OPD under different wavelengths were further investigated at 0 V. Additionally, optoelectronic properties of rigid OPD with conventional rigid electrodes ITO/Ag were fabricated and characterized for comparison (Figure 2b). *R* is a key parameter to evaluate optoelectronic conversion capability of a photodetector, which is defined by equation $R = I_{ph}/PS$, where I_{ph} represented the photocurrent of photodetector, *P* is the power density, and *S* is the effective area of the photodetector. Detectivity (*D*) indicates the capacity of the photodetector to detect weak signals and can be calculated by *R*, $D = R/(2qJ_d)^{1/2}$, where *q* is the electronic charge and J_d is the dark-current density.[29]

Photocurrent and dark current of the two devices were acquired by the current–time (*I*–*t*) response test under illumination of different wavelengths on–off at 0 V. It is found in Figure 2c,d that both the all-OPD and the rigid OPD could achieve a high *R* of about 20–150 mA W^{-1}. Especially, the all-OPD achieved its highest *R* between 500 and 600 nm, which would be beneficial to be applied in photo-plethysmography (PPG) technology for the detection of biosignals. In addition, it was found that the all-OPD depicted a lower *R* than that in rigid-OPD, and there may be two reasons. It may correspond to the limited driving force from the symmetrical electrodes PH1000/PH1000 for promoting carrier's transportation. Also, the quality of organic layers on ultraflexible substrate would decline to some extent; thus, the charge recombination may happen before they separated. Compared to the nearly transparent top PH1000/PEIE[26] (Figure 1d), there was an intense absorption of Ag over the wavelength of 400 nm,[30] which caused a large energy loss by the electrode Ag reflection or absorption thus leading to the reduction of photocurrent (Figure S4, Supporting Information) and suppression of *R* in wavelength between 400 and 600 nm for ITO/Ag-based rigid devices. *D* of the two devices exhibited the same variation trends as *R*, while there was also a slight loss of *D* in the all-OPD as a result of its higher dark current. Further, the response speed of P3HT:PC71BM-based OPD at 0 V was conducted, and it was found that steady and regular current signals under the transient light response without applied bias could be outputted, as shown in Figure S5 (Supporting Information). The response time was estimated to be 0.5 ms to rise and 3.2 ms to fall, which could satisfy the requirements of detecting of biosignals in this work.

In order to make an intensive comprehend of the internal recombination mechanism in photodetectors, photocurrent–power density (*I*–*P*) curves were plotted and fitted according to the equation $P = AI^{\alpha}$, as shown in Figure 2g. Photocurrents here were obtained from *I*–*t* curves of devices under different

light intensity illuminations of 350 nm at 0 V (Figure 2e,f) by ignoring the dark current. The exponent in the PH1000/PH1000-based all-OPD (0.85) was slightly lower than that in ITO/Ag-based OPD (0.92), which signified more bimolecular recombination. Additional defects may inevitably be brought in the preparation process of PH1000 electrodes, which was consistent with the higher dark current in the PH1000/PH1000-based all-OPD.[31] It was noted that there was a small deviation of data points to the fitting line when the power density was below 100 μW cm^{-2} because the values of photocurrent and the dark current were basically in the same order of magnitude, and the dark current cannot be ignored under weak light.

An ultraflexible self-powered all-OPD with high *R* and *D* around 500–600 nm has been fabricated through electrodes design, which has comparable optoelectronic performance with the corresponding rigid OPD. Surprisingly, it was found that the symmetrical transparent electrodes endowed the all-OPD with distinctive optoelectronic properties that the photocurrent polarity and value were dependent on the device rotating angles. As shown in **Figure 3**a, as the all-OPD was

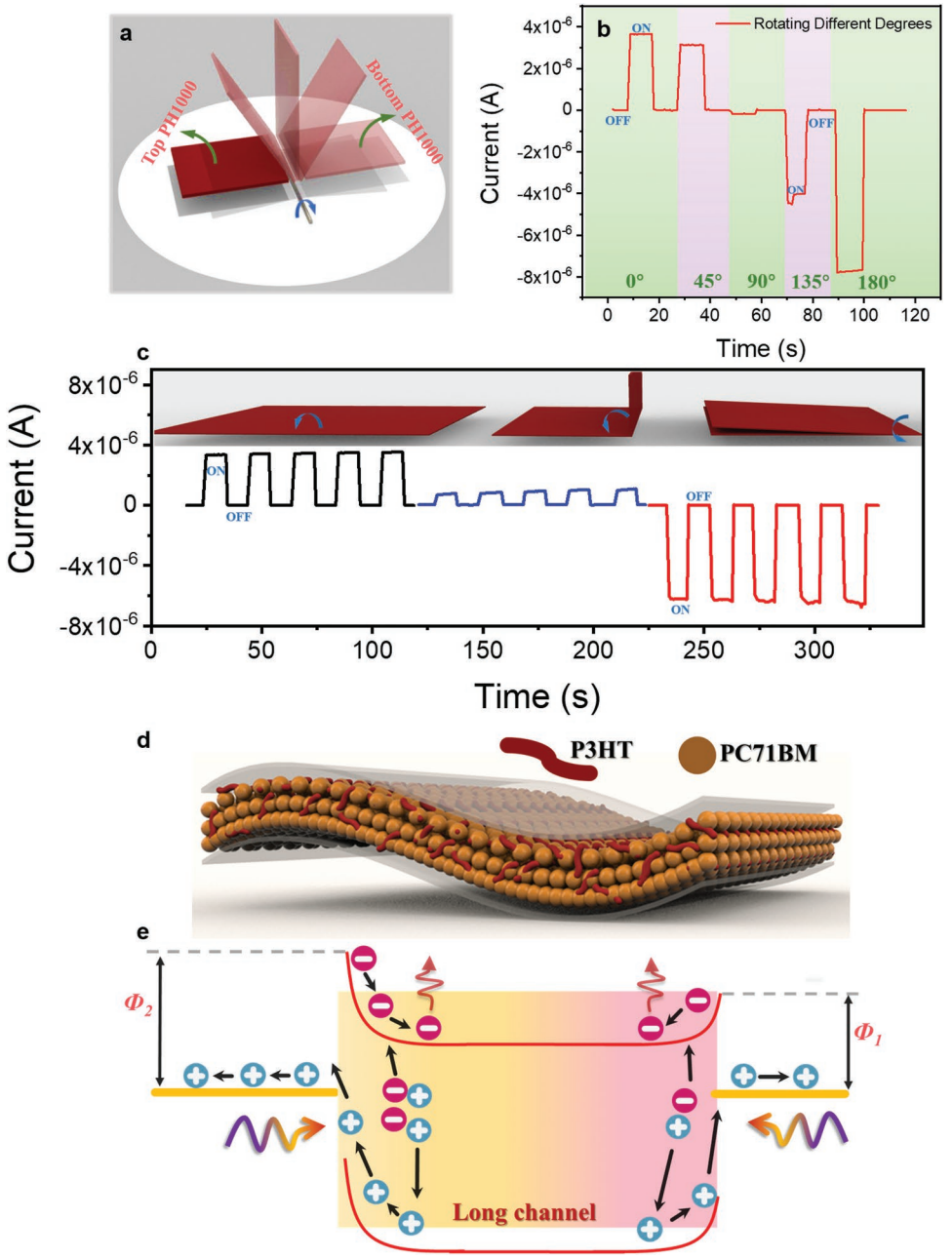

Figure 3. Dual-polarity photocurrent response and working principles of the all-OPD during flipping and folding. a) Schematic of device flipping. b) *I*–*t* output as the all-OPD flipped from 0° to 180°. c) *I*–*t* output as the all-OPD folded from 0° to 180°. The *I*–*t* curves were conducted under simulated sunlight (175 mW cm^{-2}) at 0 V. d) Distribution of donors and accepters in BHJ. e) Working principles of the dual-polarity output all-OPD as incident light illuminated from top PH1000 (the right half part) and bottom PH1000 (the left half part).

flipped from 0° to 90°, the photocurrent decreased from 4 μA to nearly zero, which may owe to the reduction of illumination area (Figure 3b). Then, when we continued flipping the device over 90°, the polarity of photocurrent switched and the value of photocurrent increased from nearly zero to a maximum value of 8 μA, as the device was completely flipped (180°). This unique performance may help establish the dependence curve between photocurrents and angles (between incident light and the all-OPD), which would have possible application in position monitoring by detecting incident light orientation. Compared with the unipolar photodetectors that can only output photocurrent on one side or output symmetrical photocurrents on both sides, this all-OPD could broaden detecting angles of incident light from 90° to 180° by outputting switchable polarity electrical signals.

Notably, considering the ultraflexibility of this all-OPD, we further explored the photocurrent output responses as it was folded to 0°, 90°, and 180°. As demonstrated in Figure 3c, the photocurrent of the all-OPD decreased to a minimum, as it was folded to 90° because almost half of the device was parallel to incident light under this circumstance. Then, as this all-OPD continued to be folded to 180°, the polarity of photocurrent was switched, and the photocurrent value of the fully folded device increased to more than 6 μA. The inside reason was that when the all-OPD was fully folded (180°), the incident light was switched to be irradiated from the bottom PH1000, hence, presented a similar switchable photocurrent polarity effect. Multifunctional properties of ultraflexibility and dual-polarity response were realized based on our fabricated all-OPD. The photocurrent polarities were strongly dependent on the folding angles of the all-OPD, which may have application prospect in the motion detection field.

Unlike conventional dual-polarity p–n junction inorganic photodetector, the switchable photocurrent in the all-OPD was intensely connected with the distinctive BHJ structure of polymer donor P3HT and fullerene acceptor PC71BM. It is found that in the polymer:fullerene system, blend properties may vary spatially perpendicular to substrate via self-assembly.[23,32] Due to the vertical phase segregation of the polymer and fullerene, PC71BM tended to concentrated at the bottom PH1000/PEDOT:PSS interface and P3HT tended to accumulated at the PEIE/top PH1000 interface.[33] However, since the mass ratio of the PC71BM and P3HT was 1.5:1 in this work, PC71BM remained dominated in the BHJ perpendicular to the substrate, as schematically shown in Figure 3d, and may form Schottky barriers after contacting electrode PH1000. While Schottky barrier height (SBH) in bottom PH1000/BHJ interface was larger than that in BHJ/top PH1000 because PC71BM was more enriched close to the substrate. Further, schematic energy level alignment diagrams of the generated electric field at the bottom PH1000/BHJ and BHJ/top PH1000 interfaces were made to help better understand carrier's migrations, as shown in Figure S6 (Supporting Information). When incident light was illuminated from top PH1000 side (Figure 3e), photogenerated excitons were stimulated at the shallow layer of the BHJ surface. Electrons and holes separated under the driving forces from donor–acceptor phase interfaces and Schottky junction, where electrons flowed to bottom PH1000 electrode and would be trapped in the thick BHJ film (≈500 nm) with the long channel. Simultaneously, sufficient holes could be transported from semiconductors to top PH1000 electrode with tunneling or thermionic injection without trapped through an ultrathin (10 nm) PEIE layer and were collected by external circuit thus outputting forward photocurrent.[28] Similarly, as incident light was illuminated from bottom PH1000 side (Figure 3e), electrons would migrate to top PH1000 electrode and then trapped in thick BHJ film, while holes would flow to bottom PH1000 and collected by external circuit, ultimately outputting reverse photocurrent. The difference, higher Schottky barrier ($\Phi_2 > \Phi_1$) in bottom PH1000/BHJ interface, could accelerate charge separation and promote more holes to flow to bottom PH1000; therefore, it will output higher reverse photocurrents as the all-OPD was completely flipped or folded.

To present a comprehensive understanding of the internal mechanism of the dual-polarity outputted photocurrent of our all-OPD. We further adjusted the work function of the top electrode by doping silver nanowires (AgNWs) to construct OPDs with asymmetric counter electrode. As AgNWs were introduced to replace half of the top PH1000 electrode (PH1000:AgNWs), device outputted a high photocurrent of over 3 μA (**Figure 4**a). The slight decrease of current compared with that in the all-OPD may be due to the higher roughness of the top PH1000:AgNW electrodes with a lower charge collection efficiency (Figure S7, Supporting Information). Similarly, when AgNWs completely replaced PH1000 as the top electrode, it was found that ideal AgNWs' conductive networks were difficult to be built on the organic surface thus outputting the lowest current (Figure 4a). Meanwhile, the minimal exponent (0.66) in PH1000/AgNW-based device implied more bimolecular recombination, which would result in the loss of photocurrent (Figure S8, Supporting Information). Consequently, the huge photocurrent difference directly influenced the *R* of PH1000/PH1000:AgNW-based and PH1000/AgNW-based devices (Figure 4b).

To investigate the relationship of photocurrent polarity with the work function of electrodes, additional *I*–*t* experiments were conducted by flipping the OPDs with PH1000/PH1000:AgNWs and PH1000/AgNWs as electrodes. When AgNWs (work function = 4.2 eV)[34] were introduced, surface potential of top electrode dropped from 5.1 eV (PH1000) to 4.8 eV(PH1000:AgNWs) (Figure S9, Supporting Information), and there was still a photocurrent polarity reverse as the device was flipped to over 90° (Figure 4c), where Schottky barrier in BHJ/top PH1000:AgNWs' interface (Φ_3) was nearly the same as Φ_1 therefore had the same mechanism as in PH1000/PH1000-based system (Figure 4d). However, as the top electrode was completely substituted by AgNWs, dual-polarity photocurrent response disappeared as it was flipped from 0° to 180° (Figure 4e). In this PH1000/AgNW-based OPD, Schottky barrier was much lower in BHJ/top AgNWs' interface (Φ_4) than that in bottom PH1000/BHJ interface (Φ_2), as incident light was illuminated from top AgNW electrode, larger amount of electrons would easily get over the Schottky barrier (Φ_4) and collected by external circuit than holes; thus, the polarity of net photocurrent became reversed as well (Figure 4f).

The mechanical bending test was of great significance in evaluating the ultraflexible all-OPD, as demonstrated in **Figure 5**a. A stable photocurrent could be outputted and remained to be about 5 μA after the all-OPD was bent for 20 000 circles. Small

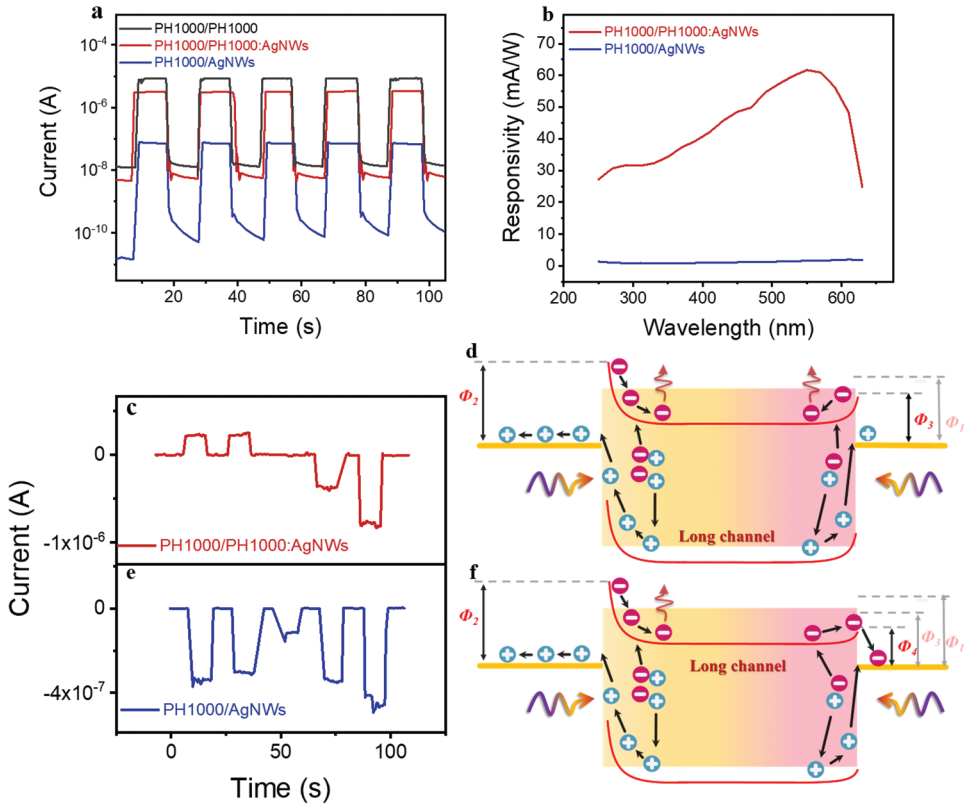

Figure 4. Optoelectronic properties and mechanisms of OPDs by varying work functions of top electrodes. a) *I–t* curves of OPDs with PH1000, PH1000:AgNWs, and AgNWs as top electrodes, under 500 nm illumination at 0 V. b) *R*s of OPDs with PH1000:AgNWs and AgNWs as top electrodes. c,d) *I–t* output as the OPDs flipped from 0° to 180° with PH1000:AgNWs (c) and AgNWs (e) as top electrodes. d,f) Working principles as incident light illuminated from top electrode (the right half part) and bottom electrode (the left half part) of different outputs in OPDs with PH1000:AgNWs (d) and AgNWs (f) as top electrodes. *I–t* tests conducted under simulated sunlight (175 mW cm^{-2}) on–off switch at 0 V.

current spikes could arise as the incident light was switching on without an external potential, which is corresponding to the photogenerated carriers stimulated at the interface rapidly without recombining in time, thus resulting in a decaying of photocurrent.[35,36] Variation of photocurrents with bending times is displayed in detail in Figure 5b; photocurrent dropped about 20% after bending 5000 times due to the morphology damage under the constant and cyclic bending stress. The photocurrents of the all-OPD would maintain at 80% of its original value as it was further bent to 20 000 circles. The physical pictures of ultraflexible all-OPD in twisted, crimped, and folded states are also shown in Figure 5b. Therefore, our designed all-OPD had great bending resistance, which was promising to work efficiently in continuous bending operation. In addition, as shown in Figure S10 (Supporting Information), the performance of our fabricated all-OPD after it was put in the air for 10 days was monitored, where the dark current and photocurrent were almost the same with the original results, which could eliminate the possibility of the device performance degradation arising from the environment.

In order to demonstrate the applicability in wearable electronics, transmission mode PPG was assembled by a red LED and our fabricated ultraflexible all-OPD, as shown in Figure 5c,d. The red LED was stuck on fingernail, which would emit red light that easily passed through the finger. The ultraflexible all-OPD was stuck on the finger pulp to detect the changes of optical signals caused by changes of blood vessel volume in the microvascular bed of tissues, which could evaluate cardiopulmonary function of humans.[37] Finally, Figure 5e depicts that 18 periodic biological signals were stably output within 15 s, indicating that this wearable self-powered all-OPD would be an outstanding candidate for all-day health monitoring.

3. Conclusion

The utilization of organic electrodes PH1000/PH1000 endows the all-OPD with ultraflexibility and achieves a self-powered *R* of over 100 mA W^{-1}, which is nearly equivalent to that of rigid OPD with ITO/Ag electrodes. Meanwhile, the device output dual-polarity photocurrent response, when it was flipped or folded, was mainly attributed to the adoption of the thick BHJ structure and transparent symmetrical electrodes. Excitons are produced on the shallow layer of illumination surface, then separated and flowed to the nearer electrode as it was flipped or folded. Moreover, this device has great bending resistance, which can maintain more than 80% of the performance after folding 20 000 times. This soft all-OPD can be applied in comfortable PPG to accurately output stable biosignals.

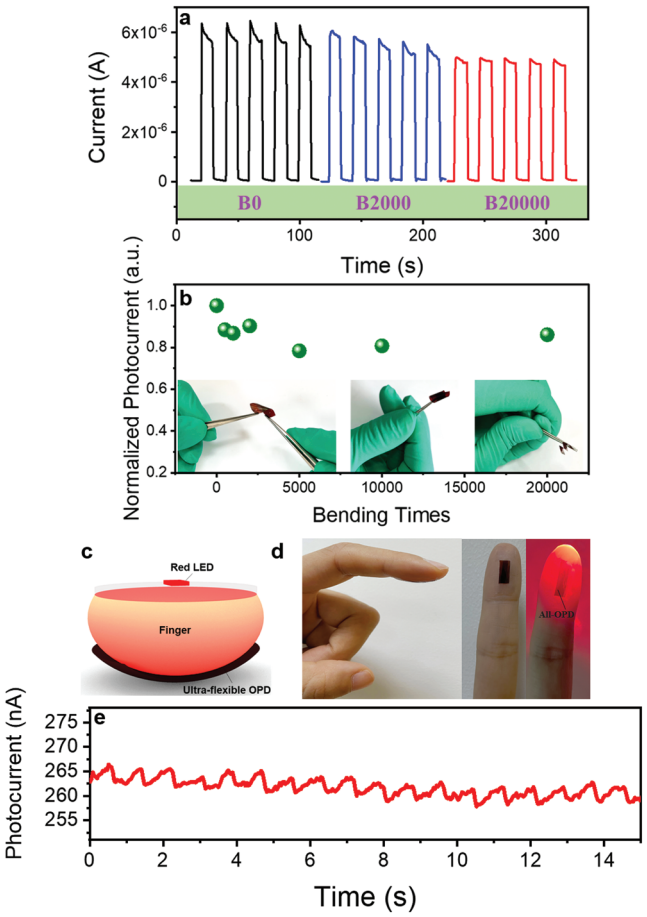

Figure 5. Optoelectronic properties of the all-OPD after a constant bending test and output signals of PPG. a) *I–t* curves of the all-OPD after bending 0 time (black line), 2000 times (blue line), and 20 000 times (red line), the bending radius was about 3 mm. b) Variation of normalized photocurrent after bending different times and physical pictures of all-OPD. *I–t* tests conducted under simulated sunlight (175 mW cm^{-2}) on–off switch at 0 V. c) Schematic and d) physical pictures of PPG based on the all-OPD. e) Outputting photocurrent of the PPG within 15 s. The power of the red LED was 0.2 W.

The whole device fabrication process only involves solution methods, which are potential for large-area production. Apart from the application scenarios discussed above, it is believed that this work will inspire researchers to develop multi-functional optoelectronic devices based on this all-OPD with dual-polarity response and excellent mechanical flexibility.

4. Experimental Section

Materials: All solvents were purchased from Sinopharm China. P3HT and PC71BM were purchased from J&K Chemicals Inc. PEDOT:PSS (Clevios P VP Al 4083) and PH1000 (Clevios PH1000) with a solid content of 1.0–1.3% were purchased from Heraeus, Inc., Germany. 2,9-dimethyl-4,7-diphenyl-1,10-phenanthroline (BCP) and PEIE were purchased from Sigma–Aldrich. The ITO-coated substrates were purchased from Youxuan, Liaoning Co., Ltd.

Device Fabrication: 32 mg of P3HT and 48 mg of PC71BM were dissolved in 1 mL of chloroform and stirred overnight at 55 °C to form a blended solution. PEIE was dissolved in dimethoxy ethanol to obtain 1 wt% PEIE solution. The volume of PH1000 and PEDOT:PSS aqueous solution was diluted with ethanol to three times the original volume before used. To fabricate a flexible device, PH1000 was sprayed on the ultrathin (30 µm) PET, which was on a 120 °C hot plate to form a 300 nm film and annealed for 20 min. Thin film of PEDOT:PSS (15 nm) was further produced in the same way as on smooth PH1000 surface. P3HT:PC71BM solution was then spin-coated and baked at 100 °C to form an active layer of about 500 nm. PEIE was sprayed on the active layer to form a thin film of about 10 nm. At last, PH1000 was sprayed on PEIE on a 120 °C hot plate and annealed at 120 °C for 20 min to form a 300 nm film. For the convenience of the optoelectronic measurements, the organic electrodes were extracted by stretchable silver paste. To fabricate a rigid device, glasses with ITO were ultrasonically cleaned with soapy water, deionized water, acetone, and isopropanol for 20 min and plasma treatment for 5 min before use. PEDOT:PSS was spin-coated on the substrate at 3000 rpm and annealed at 120 °C for 20 min. P3HT:PC71BM solution was then spin-coated and baked at 100 °C to obtain the active layer. 10 nm BCP film and 20 nm Ag film were finally prepared via vacuum thermal deposition. The PH1000, PEDOT:PSS, and PEIE layers were fabricated in the air. The photosensitive layer P3HT:PC71BM was fabricated in the glove box with nitrogen. All characterizations of the devices were conducted in the air condition. The dimensions of all devices were 0.2 cm × 0.2 cm.

Device Characterization: The transmittance of electrodes was calculated by a UV–vis spectrophotometer (Hitachi U-4100). Surface morphology and Kelvin probe were carried out using a Bruker dimension edge microscope. The optoelectronic parameters of photodetectors were investigated by Keithley 4200 with the light source system consisting of an Xe lamp and a monochromator. A transient light response system with a neodymium-doped yttrium aluminum garnet (Nd:YAG) laser (Continuum Electro-Optics, MINILITE II, pulse duration: 3–5 ns, 355 nm), a resistor, and an oscilloscope (Tektronix MSO/DPO5000) were employed to collected the pulse response data. High-resolution image of BHJ was conducted by transmission electron microscopy (TEM) (JOEL JEM-2100F).

Supporting Information

Supporting Information is available from the Wiley Online Library or from the author.

Acknowledgements

The work was supported by National Key R&D Program of China (Program No. 2017YFA0204600), the Inner Mongolia Talent Fund, National Natural Science Foundation of China (Grant Nos. 12061131009 and 51872050), and Science and Technology Commission of Shanghai Municipality (Grant Nos. 21520712600 and 19520744300). The skin-attachment experiments displayed in Figure 5 did not require ethics board approval and all participants took part as volunteers following assessment of any risks and informed consent.

Conflict of Interest

The authors declare no conflict of interest.

Data Availability Statement

Research data are not shared.

Keywords

all-organic photodetectors, all-solution processing method, biosignal detection, dual-polarity output

Received: February 9, 2022
Revised: April 17, 2022
Published online: June 22, 2022

[1] N. Matsuhisa, S. Niu, S. J. K. O'Neill, J. Kang, Y. Ochiai, T. Katsumata, H.-C. Wu, M. Ashizawa, G.-J. N. Wang, D. Zhong, X. Wang, X. Gong, R. Ning, H. Gong, I. You, Y. Zheng, Z. Zhang, J. B.-H. Tok, X. Chen, Z. Bao, *Nature* **2021**, *600*, 246.
[2] J. Mun, Y. Ochiai, W. Wang, Y. Zheng, Y. Q. Zheng, H. C. Wu, N. Matsuhisa, T. Higashihara, J. B. Tok, Y. Yun, Z. Bao, *Nat. Commun.* **2021**, *12*, 3572.
[3] S. Park, S. W. Heo, W. Lee, D. Inoue, Z. Jiang, K. Yu, H. Jinno, D. Hashizume, M. Sekino, T. Yokota, K. Fukuda, K. Tajima, T. Someya, *Nature* **2018**, *561*, 516.
[4] Y. Zheng, Z. Yu, S. Zhang, X. Kong, W. Michaels, W. Wang, G. Chen, D. Liu, J. C. Lai, N. Prine, W. Zhang, S. Nikzad, C. B. Cooper, D. Zhong, J. Mun, Z. Zhang, J. Kang, J. B. Tok, I. McCulloch, J. Qin, X. Gu, Z. Bao, *Nat. Commun.* **2021**, *12*, 5701.
[5] J. Anthony, A. Facchetti, M. Heeney, S. R. Marder, X. Zhan, *Adv. Mater.* **2010**, *22*, 3876.
[6] P. C. Y. Chow, T. Someya, *Adv. Mater.* **2020**, *32*, 1902045.
[7] H. Huang, L. Jiang, J. Peng, Y. Qi, S. Bai, Q. Lin, *Chem. Mater.* **2021**, *33*, 8089.
[8] Y. Xia, L. E. Aguirre, X. Xu, O. Inganäs, *Adv. Electron. Mater.* **2020**, *6*, 1901017.
[9] X. Xu, X. Zhou, K. Zhou, Y. Xia, W. Ma, O. Inganäs, *Adv. Funct. Mater.* **2018**, *28*, 1805570.
[10] C. Fuentes-Hernandez, W.-F. Chou, T. M. Khan, L. Diniz, J. Lukens, F. A. Larrain, V. A. Rodriguez-Toro, B. Kippelen, *Science* **2020**, *370*, 698.
[11] B. Park, J. Jung, D. H. Lim, H. Lee, S. Park, M. Kyeong, S. J. Ko, S. H. Eom, S. H. Lee, C. Lee, S. C. Yoon, *Adv. Funct. Mater.* **2021**, *32*, 2108026.
[12] J. H. Kim, A. Liess, M. Stolte, A. M. Krause, V. Stepanenko, C. Zhong, D. Bialas, F. Spano, F. Wurthner, *Adv. Mater.* **2021**, *33*, 2100582.
[13] J. Huang, J. Lee, J. Vollbrecht, V. V. Brus, A. L. Dixon, D. X. Cao, Z. Zhu, Z. Du, H. Wang, K. Cho, G. C. Bazan, T. Q. Nguyen, *Adv. Mater.* **2020**, *32*, 1906027.
[14] H. Jinno, T. Yokota, M. Koizumi, W. Yukita, M. Saito, I. Osaka, K. Fukuda, T. Someya, *Nat. Commun.* **2021**, *12*, 2234.
[15] T. Yokota, T. Nakamura, H. Kato, M. Mochizuki, M. Tada, M. Uchida, S. Lee, M. Koizumi, W. Yukita, A. Takimoto, T. Someya, *Nat. Electron.* **2020**, *3*, 113.
[16] B. Ouyang, Y. Wang, R. Zhang, H. Olin, Y. Yang, *Cell Rep. Phys. Sci.* **2021**, *2*, 100418.
[17] D. Wang, X. Liu, Y. Kang, X. Wang, Y. Wu, S. Fang, H. Yu, M. H. Memon, H. Zhang, W. Hu, Z. Mi, L. Fu, H. Sun, S. Long, *Nat. Electron.* **2021**, *4*, 645.
[18] B. Ouyang, K. Zhang, Y. Yang, *iScience* **2018**, *1*, 16.
[19] B. Ouyang, H. Zhao, Z. L. Wang, Y. Yang, *Nano Energy* **2020**, *68*, 104312.
[20] C. V. Hoang, K. Hayashi, Y. Ito, N. Gorai, G. Allison, X. Shi, Q. Sun, Z. Cheng, K. Ueno, K. Goda, H. Misawa, *Nat. Commun.* **2017**, *8*, 771.
[21] X. Lu, P. Jiang, X. Bao, *Nat. Commun.* **2019**, *10*, 138.
[22] A. Wadsworth, Z. Hamid, J. Kosco, N. Gasparini, I. McCulloch, *Adv. Mater.* **2020**, *32*, 2001763.
[23] Z. Xu, L.-M. Chen, G. Yang, C.-H. Huang, J. Hou, Y. Wu, G. Li, C.-S. Hsu, Y. Yang, *Adv. Funct. Mater.* **2009**, *19*, 1227.
[24] C. Hsieh, Y. Cheng, P. Li, C. Chen, M. Dubosc, R. Liang, C. Hsu, *J. Am. Chem. Soc.* **2010**, *132*, 4887.
[25] N. Ali, M. Michelle, T. Dattatray, P. Sreelekha, K. Anshu, K. Anil, B. Hrishikesh, P. Amlan, H. Ivo, *Org. Electron.* **2016**, *38*, 89.
[26] S. Xiong, L. Hu, L. Hu, L. Sun, F. Qin, X. Liu, M. Fahlman, Y. Zhou, *Adv. Mater.* **2019**, *31*, 1806616.
[27] B. Xu, J. Hou, *Adv. Energy Mater.* **2018**, *8*, 1800022.
[28] Y. Zhou, C. Fuentes-Hernandez, J. Shim, J. Meyer, A. J. Giordano, H. Li, P. Winget, T. Papadopoulos, H. Cheun, J. Kim, M. Fenoll, A. Dindar, W. Haske, E. Najafabadi, T. M. Khan, H. Sojoudi, S. Barlow, S. Graham, J.-L. Brédas, S. R. Marder, A. Kahn, B. Kippelen, *Science* **2012**, *336*, 327.
[29] F. Teng, K. Hu, W. Ouyang, X. S. Fang, *Adv. Mater.* **2018**, *30*, 1706262.
[30] T. Yan, S. Cai, Z. Hu, Z. Li, X. S. Fang, *J. Phys. Chem. Lett.* **2021**, *12*, 9912.
[31] J. Kublitski, A. Hofacker, B. K. Boroujeni, J. Benduhn, V. C. Nikolis, C. Kaiser, D. Spoltore, H. Kleemann, A. Fischer, F. Ellinger, K. Vandewal, K. Leo, *Nat. Commun.* **2021**, *12*, 551.
[32] M. Campoy-Quiles, T. Ferenczi, T. Agostinelli, P. G. Etchegoin, Y. Kim, T. D. Anthopoulos, P. N. Stavrinou, D. D. Bradley, J. Nelson, *Nat. Mater.* **2008**, *7*, 158.
[33] D. M. N. M. Dissanayake, A. Ashraf, Y. Pang, M. D. Eisaman, *Adv. Energy Mater.* **2014**, *4*, 1300525.
[34] W. Yang, Y. Zhang, Y. Zhang, W. Deng, X. S. Fang, *Adv. Funct. Mater.* **2019**, *29*, 1905923.
[35] X. Deng, Z. Li, H. Liu, Y. Zhao, L. Zheng, X. Shi, L. Wang, X. S. Fang, H. Zheng, *Small* **2021**, *17*, 2101674.
[36] H. Fang, C. Zheng, L. Wu, Y. Li, J. Cai, M. Hu, X. S. Fang, R. Ma, Q. Wang, H. Wang, *Adv. Funct. Mater.* **2019**, *29*, 1809013.
[37] H. Lee, E. Kim, Y. Lee, H. Kim, J. Lee, M. Kim, H.-J. Yoo, S. Yoo, *Sci. Adv.* **2018**, *4*, 9530.

